

## Special Section: Nonuniform Flow across Vadose Zone Scales

### Core Ideas

- We present a cost-effective and simple method for dual-permeability model parameterization.
- Physical characterization is done with only experimental results of saturated flow experiments.
- Model inputs require only saturated flow results with water and a non-Newtonian fluid.

C.N. Basset, M.R. Abou Najm, A. Ammar, and G. Saad, Civil & Environmental Engineering, American Univ. of Beirut, Beirut, Lebanon; M.R. Abou Najm, Land, Air and Water Resources, Univ. of California at Davis, Davis, CA 95616; R.D. Stewart, School of Plant and Environmental Sciences, Virginia Polytechnic Institute and State Univ., Blacksburg, VA 24061; S.C. Hauswirth, California State Univ., Geological Sciences, Northridge, Northridge, CA 90802. \*Corresponding author (mabounajm@ucdavis.edu).

Received 15 Sept. 2018.

Accepted 15 Apr. 2019.

Supplemental material online.

Citation: Basset, C.N., M.R. Abou Najm, A. Ammar, R.D. Stewart, S.C. Hauswirth, and G. Saad. 2019. Physically based model for extracting dual-permeability parameters using non-Newtonian fluids. *Vadose Zone J.* 18:180172. doi:10.2136/vzj2018.09.0172

© 2019 The Author(s). This is an open access article distributed under the CC BY-NC-ND license (<http://creativecommons.org/licenses/by-nc-nd/4.0/>).

# Physically Based Model for Extracting Dual-Permeability Parameters Using Non-Newtonian Fluids

Christelle N. Basset, Majdi R. Abou Najm,\* Ashtarout Ammar, Ryan D. Stewart, Scott C. Hauswirth, and Georges Saad

Dual-permeability models simulate flow and transport within soils characterized by preferential (macro) and matrix (micro) pore domains, with each exhibiting distinct hydraulic properties. The lack of suitable methods for determining appropriate and physically based model parameters remains a major challenge to applying these models. Here, we present a method that characterizes dual-permeability model parameters using experimental results of saturated flows from water and a non-Newtonian fluid. We present two sub-models that solve for the effective pore sizes of micropores and macropores, with macropores represented either with cylindrical (for biological pores) or planar (for shrinkage cracks and fissures) pore geometries. The model also determines the percentage contribution ( $w_i$ ) of the representative macro- and micropores to water flow. We applied the model to experimental soil samples complemented with capillary tubes simulating the macropores and showed its ability to derive the bimodal pore size distributions in dual-domain soils using only two fluids. As such, we present this method of characterization of dual structures for improved modeling of nonuniform preferential flow and transport in macroporous soils.

Abbreviations:  $\mu$ CT, X-ray microcomputed tomography.

Many soils contain complex structures such as fractures, fissures, cracks, and macropores that dissect the soil matrix. These structures form as result of multiscale complex interactions between soil physical and biogeochemical properties, moisture condition, stress level, and biological activity (Abou Najm et al., 2010) and can affect water and solute transport by creating preferential flow (Beven, 1991). During preferential flow events, nonequilibrium conditions lead to differences in water pressures and solute concentrations (Gerke and van Genuchten, 1993; Jarvis, 2007). Such features of preferential flow cannot be captured by the Richards equation based on the single-porosity approach (Beven and Germann, 1982; van Genuchten et al., 1990).

Different approaches have been proposed to describe water flow in the porous media using double-porosity or dual-permeability models (Gerke and van Genuchten, 1993; Jarvis, 1994; Šimůnek et al., 2003; Lewandowska et al., 2004). The term dual-permeability is used to characterize a porous medium composed of two subdomains with distinct pore sizes and hydraulic conductivities. For example, Gerke and van Genuchten (1993) derived two Richards' equations coupled by an exchange term to represent the water transfer between macropores in a fracture network and micropores in the soil matrix. The exchange term is proportional to the conductivity of the interface and the difference in pressure head between the two domains. Jarvis (1994) described flow in high-permeability domain by kinematic wave equation and assumed the water transfer to be proportional to the difference in relative saturations. Lewandowska et al. (2004) described flow within each domain using the Richards equation, yet their solution requires knowledge of geometry and hydraulic conductivity of the high-permeability domain.

A major challenge to using these theoretical models is that we currently have limited ability to measure or identify their required parameters (Köhne et al., 2002), especially since inverse identification of macroscopic parameters can lead to several challenges, mainly related to the instability and nonuniqueness of the parameters (Larsson and Jarvis, 1999). Non-Newtonian fluids have recently been used to characterize soil properties (Di Federico et al., 2010; Comba et al., 2011; Busch et al., 2014; Gastone et al., 2014; Stewart et al., 2014; Tosco et al., 2014), with Abou Najm and Atallah (2016) building a system of equations that abstracts the pore structure into a system of  $N$  pore groups, each having a corresponding representative pore radius ( $R_j$ ) and percentage contribution to water flow ( $w_j$ ). The model (hereafter referred to as the ANA model) requires only the experimental results of saturated flow experiments of the tested medium with water and  $N - 1$  non-Newtonian fluids. The model was tested on synthetic porous media and demonstrated its ability to extract multiple porosity-permeability domains (Atallah and Abou Najm, 2019).

Here, we use the ANA model with water and a non-Newtonian fluid in saturated flow experiments to extract the physically based parameters of dual-permeability model required for improved flow predictions. Two submodels are established to determine the effective macropore sizes assuming either cylindrical or planar pore geometries, with micropores represented by cylindrical geometry. This model also determines the percentage contribution to flow ( $w_j$ ) corresponding to the representative macro- and micropores. A user-friendly solver was developed to solve the system of equations, including numerical and analytical integration of the non-Newtonian viscosity models.

## Theory

Assuming steady-state, incompressible, saturated, and laminar flow under isothermal conditions having a generalized Newtonian viscosity models, the Navier–Stokes equations for flow in circular tubes using cylindrical coordinates reduce to

$$\frac{1}{r} \frac{d}{dr} \left( r \eta \frac{dv_z}{dr} \right) = \rho g \frac{(\partial h / \partial z) - 1}{T} \quad [1]$$

where  $r$  is the radius of the circular tube [L],  $\rho$  is the density [ $\text{M L}^{-3}$ ],  $g$  is the gravitational acceleration [ $\text{M T}^{-2}$ ],  $\eta$  is the dynamic viscosity [ $\text{M L}^{-1} \text{T}^{-1}$ ],  $dv_z/dr$  is the shear rate [ $\text{L T}^{-1}$ ],  $\partial h / \partial z$  is the pressure head gradient per unit length [ $\text{L L}^{-1}$ ], and  $T$  is the tortuosity factor [ $\text{L L}^{-1}$ ]. For horizontal flow, the right-hand side of the governing differential equation becomes equal to  $\rho g [(\partial h / \partial z) / T]$ .

Using this flow as a building block and assuming a simplified structure of parallel capillary tubes, Abou Najm and Atallah (2016) derived a  $N \times N$  square matrix that uses the saturated flow rates of  $N$  saturated flow experiments (using water and any  $N - 1$  non-Newtonian fluids) to predict a pore structure divided into a system of  $N$  pore groups, each having a corresponding representative pore radius ( $R_j$ ) and percentage contribution to water flow ( $w_j$ ):

$$\begin{bmatrix} \frac{(2\pi \int_0^{R_1} r v^{S_1} dr)}{R_1^4} & \frac{(2\pi \int_0^{R_2} r v^{S_2} dr)}{R_2^4} & \frac{(2\pi \int_0^{R_3} r v^{S_3} dr)}{R_3^4} & \dots & \frac{(2\pi \int_0^{R_N} r v^{S_N} dr)}{R_N^4} \\ \frac{(2\pi \int_0^{R_1} r v^{S_2} dr)}{R_1^4} & \frac{(2\pi \int_0^{R_2} r v^{S_2} dr)}{R_2^4} & \frac{(2\pi \int_0^{R_3} r v^{S_3} dr)}{R_3^4} & \dots & \frac{(2\pi \int_0^{R_N} r v^{S_3} dr)}{R_N^4} \\ \vdots & \vdots & \vdots & \ddots & \vdots \\ \frac{(2\pi \int_0^{R_1} r v^{S_N} dr)}{R_1^4} & \frac{(2\pi \int_0^{R_2} r v^{S_N} dr)}{R_2^4} & \frac{(2\pi \int_0^{R_3} r v^{S_N} dr)}{R_3^4} & \dots & \frac{(2\pi \int_0^{R_N} r v^{S_N} dr)}{R_N^4} \\ \frac{(2\pi \int_0^{R_1} r_1 dr)}{R_1^4} & \frac{(2\pi \int_0^{R_2} r_1 dr)}{R_2^4} & \frac{(2\pi \int_0^{R_3} r_1 dr)}{R_3^4} & \dots & \frac{(2\pi \int_0^{R_N} r_1 dr)}{R_N^4} \end{bmatrix} \begin{bmatrix} T_1 \\ T_2 \\ T_3 \\ \vdots \\ T_N \end{bmatrix} = \begin{bmatrix} Q_2 C_1 \\ Q_1 \\ Q_3 C_1 \\ \vdots \\ Q_N C_1 \\ Q_1 \\ \phi A_T C_1 \\ Q_1 \end{bmatrix} \quad [2]$$

where  $v^{S_j}$  is the velocity function for fluid  $S_j$  [ $\text{L T}^{-1}$ ],  $Q_j$  is the flow generated from the  $j$ th infiltration experiment [ $\text{L}^3 \text{T}^{-1}$ ],  $\phi$  is the porosity of the porous media [ $\text{L}^3 \text{L}^{-3}$ ],  $A_T$  is the total area of the porous media [ $\text{L}^2$ ], and

$$C_1 = \pi \frac{\alpha}{1 + 3\alpha} \left( -\frac{H}{2\beta} \right)^{1/\alpha}$$

with  $\beta$  as the consistency index in [ $\text{M L}^{-1} \text{T}^{-1}$ ],  $\alpha$  as the exponent in dimensionless units, with  $\alpha = 1$  for water, and  $H = \rho g (\partial h / \partial z - 1)$  for vertical flow or  $\rho g (\partial h / \partial z)$  for horizontal flow.

## ANA-2 Model for Dual-Permeability Soils

In this work, we use the ANA model to develop a two-by-two matrix (solving for the case of  $N = 2$ ) that can be used to extract physically based dual-permeability model parameters. We refer to this model as ANA-2 model. We simplify the pore structure into one of two configurations (Fig. 1): micropores represented by cylindrical pore geometries with macropores either in cylindrical (e.g., biological pores) or planar (e.g., shrinkage cracks and fissures) pore geometries. Detailed derivations are provided in the Supplemental Material.

In Configuration 1 (Fig. 1), the pore structure of the porous medium is abstracted into micropores with  $X_{\text{micro}}$  number of circular pores of radius  $R_{\text{micro}}$  and tortuosity ( $T_{\text{micro}}$ ), as well as into macropores with  $X_{\text{macro}}$  number of circular pores of radius  $R_{\text{macro}}$  and tortuosity  $T_{\text{macro}}$ . The circular micropores and macropores respectively contribute  $w_{\text{micro}}$  and  $w_{\text{macro}}$  portions of total flow  $Q_1$  (with  $w_{\text{micro}} + w_{\text{macro}} = 1$ ). Here,  $Q_1$  is the equilibrium saturated total flow obtained experimentally for a sample of total cross-sectional area  $A_T$  when water was the fluid tested, and  $Q_2$  is the same with the non-Newtonian fluid. The resulting system of equations is

$$\begin{aligned}
& \underbrace{\left( \frac{2\pi \int_0^{R_{\text{micro}}} v_c^{S_2} r dr}{R_{\text{micro}}^4} \right) \left( \frac{2\pi \int_0^{R_{\text{macro}}} v_c^{S_2} r dr}{R_{\text{macro}}^4} \right)}_A \\
& \underbrace{\left( \frac{T_{\text{micro}} \frac{\pi}{R_{\text{micro}}^2}}{T_{\text{macro}} \frac{\pi}{R_{\text{macro}}^2}} \right)}_w \\
& \times \left[ \frac{T_{\text{micro}} w_{\text{micro}}}{T_{\text{macro}} w_{\text{macro}}} \right] = \left[ \frac{Q_2 A_1}{Q_1} \right] \\
& \left[ \frac{\phi A_T A_1}{Q_1} \right]
\end{aligned} \quad [3]$$

where  $A_1 = \pi/4(-H_{cl}/2\mu)$ ,  $H_{cl}$  is the overall hydraulic pressure head term through the circular pores define as  $\rho g(\partial h/\partial z - 1)$  for vertical flow or  $\rho g(\partial h/\partial z)$  for horizontal flow, and  $v_c^{S_2}$  is the velocity of the non-Newtonian fluid in circular pores.

In Configuration 2 (Fig. 1), the pore structure of the porous medium is abstracted into micropores with  $X_{\text{micro}}$  number of circular pores of radius  $R_{\text{micro}}$  and tortuosity  $T_{\text{micro}}$  as well as into macropores with  $Y_{\text{macro}}$  number of linear cracks of width  $W_{\text{macro}}$ , length  $b_{\text{macro}}$ , and tortuosity  $T_{\text{macro}}$ . The circular micropores and linear macropores respectively contribute  $w_{\text{micro}}$  and  $w_{\text{macro}}$  portions of total flow  $Q_1$  (with  $w_{\text{micro}} + w_{\text{macro}} = 1$ ). Similarly,  $Q_1$  is the equilibrium saturated total flow obtained experimentally for a sample of total cross-sectional area  $A_T$  when water was the fluid tested, and  $Q_2$  is the same with the non-Newtonian fluid. The resulting system of equations is

$$\begin{aligned}
& \underbrace{\left( \frac{1}{A_1} \right) \left( \frac{2\pi \int_0^{R_{\text{micro}}} v_c^{S_2} r dr}{R_{\text{micro}}^4} \right) \left( \frac{1}{B_1} \right) \left( \frac{2 \int_0^{W_{\text{macro}}/2} v_l^{S_2} dy}{W_{\text{macro}}^3} \right)}_A \\
& \underbrace{\left( \frac{1}{A_1} \right) \left( \frac{T_{\text{micro}} \frac{\pi}{R_{\text{micro}}^2}}{T_{\text{macro}} \frac{1}{W_{\text{macro}}^2}} \right)}_w \\
& \times \left[ \frac{T_{\text{micro}} w_{\text{micro}}}{T_{\text{macro}} w_{\text{macro}}} \right] = \left[ \frac{Q_2}{Q_1} \right] \\
& \left[ \frac{\phi A_T}{Q_1} \right]
\end{aligned} \quad [4]$$

where  $B_1 = 1/6(-H_{l1}/2\mu)$ ,  $H_{l1}$  is the overall hydraulic pressure head term through the linear cracks and  $v_l^{S_2}$  is the velocity of the non-Newtonian fluid in linear cracks.

## Non-Newtonian Fluid Properties

The main inputs to the model are the total saturated flows ( $Q_1$  for water and  $Q_2$  for the non-Newtonian fluid) and the non-Newtonian fluid properties. Those properties are needed since modeling flow of non-Newtonian fluids requires the characterization of fluid viscosity before solving the flow equation on the modeled pore structure. Common viscosity models for non-Newtonian fluids are defined as follows:

$$\text{Power law } \eta = k \left( -\frac{\partial v_z}{\partial r} \right)^{\alpha-1} \quad [5]$$

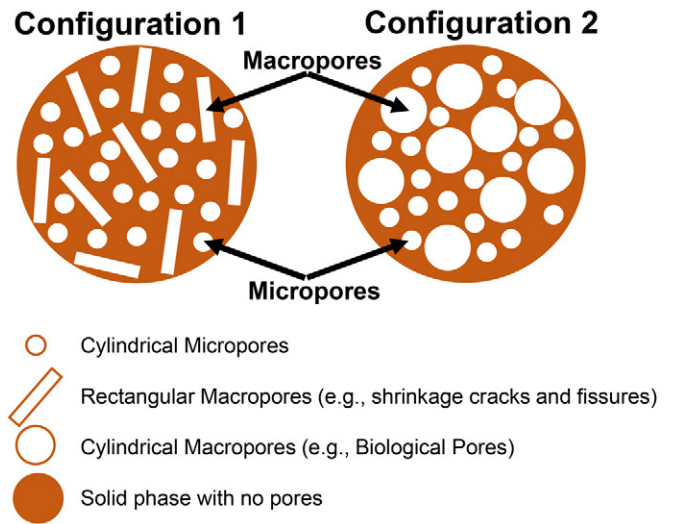


Fig. 1. The two abstractions of the pore structure in dual-structured soils.

$$\text{Cross } \eta = \eta_{\infty} + \frac{\eta_0 - \eta_{\infty}}{1 + k \left( -\partial v_z / \partial r \right)^{1-\alpha}} \quad [6]$$

$$\text{Carreau-Yasuda } \eta = \eta_{\infty} + \frac{\eta_0 - \eta_{\infty}}{\left\{ 1 + \left[ -k \left( \partial v_z / \partial r \right) \right]^{\lambda} \right\}^{(1-\alpha)/\lambda}} \quad [7]$$

$$\text{Carreau } \eta = \eta_{\infty} + \frac{\eta_0 - \eta_{\infty}}{\left\{ 1 + \left[ -k \left( \partial v_z / \partial r \right) \right]^2 \right\}^{(1-\alpha)/2}} \quad [8]$$

where  $k$  is the consistency index or the viscosity at a shear rate of  $1 \text{ s}^{-1} [\text{M L}^{-1} \text{ T}^{-1}]$ ,  $\alpha$  is the exponent in dimensionless units (1 for Newtonian,  $0 < \alpha < 1$  for shear thinning, and  $\alpha > 1$  for shear thickening fluids),  $\eta_0$  the viscosity at zero shear rate  $[\text{M L}^{-1} \text{ T}^{-1}]$ ,  $\eta_{\infty}$  the viscosity at infinite shear rate  $[\text{M L}^{-1} \text{ T}^{-1}]$ , and  $\lambda$  the relaxation time  $[\text{T}]$ .

## ANA-2 Model Solution

Similar to the ANA model, ANA-2 solves the derived system of equations to provide answers to three different problem types. A numerical solver was developed for ANA-2 using Matlab optimizer (available on request from the corresponding author). The solver numerically evaluates the ANA-2 system of equations for a dual-domain soil to answer any of the following three problem types:

- Problem Type 1: Assuming a relatively known or predefined structure represented as micropores of radius  $R_{\text{micro}}$  and tortuosity  $T_{\text{micro}}$ , as well as macropores of either circular pores of radius  $R_{\text{macro}}$  (Configuration 1) or linear cracks of width  $W_{\text{macro}}$  (Configuration 2) and tortuosity  $T_{\text{macro}}$ , what are the corresponding weights or contributions to the total water saturated flow  $Q_1$ ? Here, the model output is  $w_{\text{micro}}$  for circular micropores and  $w_{\text{macro}}$  for macropores with circular or linear configurations.
- Problem Type 2: Given predefined flow regimes (represented by weights  $w_{\text{micro}}$  for circular micropores and  $w_{\text{macro}}$  for

macropores), what are the representative pore size dimensions of the micropores and macropores that satisfy the predefined weights for the given soil? Here, the model output is the representative radius of the micropores  $R_{\text{micro}}$ , given tortuosity  $T_{\text{micro}}$ , and the representative radius of the circular macropores  $R_{\text{macro}}$  (for Configuration 1) or representative width  $w_{\text{macro}}$  of the linear cracks (for Configuration 2), given tortuosity  $T_{\text{macro}}$ .

- Problem Type 3: More generally, and given only the total saturated flows from water ( $Q_1$ ) and the non-Newtonian fluid ( $Q_2$ ). What is an optimum and representative pore dual structure that can represent the soil sample and what are the corresponding contributions to flow for each of the micro- and macropores? The model output is the representative radius  $R_{\text{micro}}$  and contribution to flow  $w_{\text{micro}}$  of the micropores, and  $R_{\text{macro}}$  (circular configurations) or  $W_{\text{macro}}$  (linear configurations) and contribution to flow  $w_{\text{macro}}$  for macropores. At this level, the model retrieves four unknowns using a system of two equations. To perform this evaluation, the approach was further presented and validated in the methods and results analysis.

## Tortuosity

The soil structure is a complex and highly interconnected network of three-dimensional pores. Representing such complexities with dual structures or one-dimensional bundles of capillary tubes may be practical for some soil applications but surely does not satisfy all soil structures. To account for some of the structural complexities that are beyond the capabilities of the simple model of parallel tubes, the model can describe different tortuosities for each of the dual structures. Tortuosity is defined as the ratio of the actual distance traveled by a fluid through the pore structure ( $l_c$ ) to the straight line distance ( $l$ ) crossing the porous medium (i.e.,  $T = l_c/l$ ; Moldrup et al., 2001). It is commonly characterized by the porosity of the porous medium with a typical range between 1.2 and 3 but can reach values as high as 50 for low-porosity media (Matyka et al., 2008). However, Carey et al. (2016) indicated that total porosity is a poor predictor for tortuosity coefficient and suggested hydraulic conductivity as a more reliable predictor for tortuosity. A comprehensive summary of different theoretical and experimental attempts to define hydraulic tortuosity is shown in Table 1.

## Methods

We assess the ANA-2 model's ability to identify dual structural characteristics of porous media to aid dual-permeability models in identifying micropore and macropore flow characteristics and parameters. To achieve this, ANA-2 model predictions were compared with experimental results of engineered dual-domain structures.

## Experimental Setup

To perform infiltration experiments, a Darcian flow setup was constructed to accommodate two distinct fluids and the test samples (Fig. 2). The system comprised two reservoirs to ensure the two fluids' supply (water and non-Newtonian fluid), a hydraulic pump to maintain constant head, a piezometer to record the pressure head, and shutoff and control valves to adjust the flow and an outlet to collect the fluid once the outflow reaches a steady state regime.

Soils tested included three standard silica sands representing the matrix flow (micropores) coupled with different numbers of capillary tubes representing preferential flow (macropores). The three silica sands and their corresponding porosities were: no. 12/20 ( $\phi = 0.35$ ), no. 20/30 ( $\phi = 0.34$ ), and no. 40/50 ( $\phi = 0.33$ ). The sample no. 12/20 represents the silica sand particles passing sieve no. 12 with 1.7-mm openings and retained on sieve no. 20 with 0.85-mm openings. This definition similarly applies for the samples no. 20/30 and no. 40/50, given that sieves no. 30, no. 40, and no. 50 have respective openings of 0.6, 0.42, and 0.3 mm. Capillary tubes of 0.75-mm radius and 7.5-cm length were used to represent the macropores. The capillary tubes were inserted vertically along the direction of the flow as one, two, or three capillary tubes of 0.75-mm radius. Infiltration tests were performed in a 50-cm-high by 2.8-cm-i.d. tube, in which silica sand was packed to a height of 6 cm. The 6-cm sand columns were supported from the bottom by a mesh fixed to a perforated Plexiglas sheet of 2.7-cm diam. and 1.5-cm thickness, used to sustain the 7.5-cm-long capillary tubes. This sheet was held by another circular plate of 2.5 cm, perforated at the middle to allow water or non-Newtonian fluids to flow from the pipe into the porous medium. Both sheets were attached with O-rings to restrict drainage. To prepare the soil sample, the procedure below was followed.

Table 1. Summary of common hydraulic tortuosity ( $T$ )–porosity ( $\phi$ ) relations.

| Reference                      | Relation  | Type of soil                                   | Method of analysis | Range of $T$ for $0.2 \leq \phi \leq 0.6$ |
|--------------------------------|---|--|--------------------|---|
| Carman (1937)                  | $T = 2$   | equal-sized spheres                            | theoretical        | 2   |
| Dullien (1975)                 | $T = 3$   | parallel capillary model                       | theoretical        | 3   |
| Berryman (1981)                | $T = (1 + 1/\phi)/2$                                      | fully consolidated granular constituents       | theoretical        | $1.3 \leq T \leq 3$                       |
| Du Plessis and Masliyah (1991) | $T = \phi/[1 - (1 - \phi)^{2/3}]$                         | isotropic granular media                       | analytical         | $1.3 \leq T \leq 1.5$                     |
| Mauret and Renaud (1997)       | $T = 1 - 0.49 \ln(\phi)$                                  | packed beds with spherical particles           | empirical          | $1.1 \leq T \leq 1.4$                     |
| Mota et al. (2001)             | $T = \phi^{-0.4}$   | spherical particles                            | empirical          | $1.2 \leq T \leq 1.9$                     |
| Ahmadi et al. (2011)           | $T = \sqrt{\{2\phi/3[1 - 1.209(1 - \phi)^{2/3}]\} + 1/3}$ | mono-sized spherical particles $\phi \geq 0.3$ | theoretical        | $1.2 \leq T \leq 2.2$                     |
| Duda et al. (2011)             | $T = 1 + (1 - \phi)^{1/2}$                                | freely overlapping squares                     | empirical          | $1.6 \leq T \leq 1.9$                     |



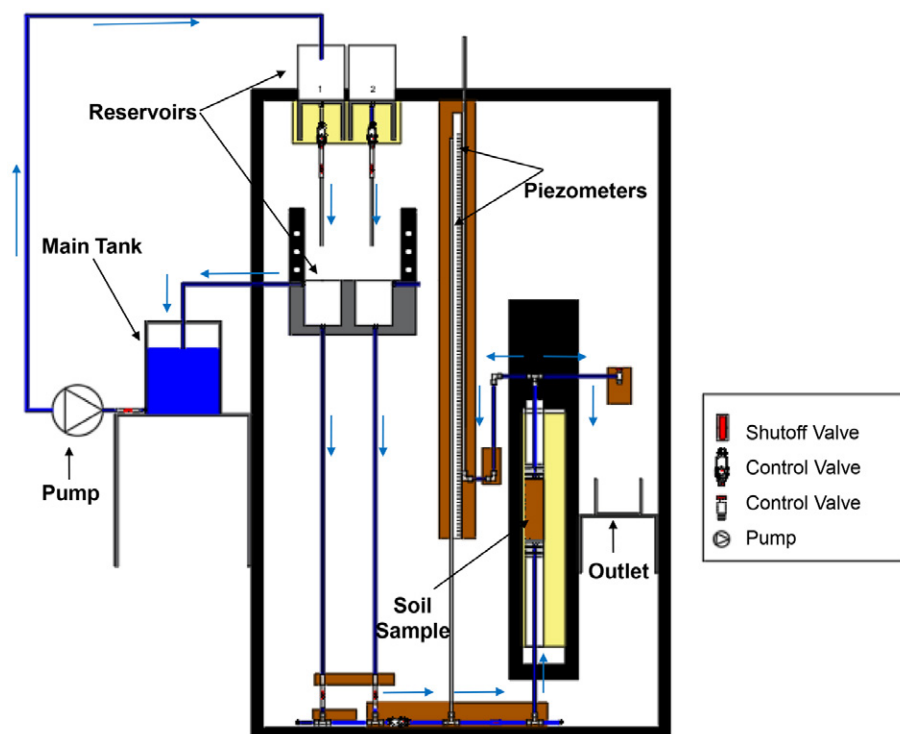


Fig. 2. Infiltration apparatus for the constant pressure head experiment.

First, the capillary tubes were fixed to a perforated Plexiglas sheet of 2.7-cm diam. and 1.5-cm thickness and clogged with temporary filaments. Then, the capillary tubes were put in place, and sand was poured layer by layer until the 6-cm column is completely covered. Note that the height of the capillary tube was equal to the height of the sand column plus the thickness of the Plexiglas sheets. Once sand was poured, the filaments were removed from the capillary tubes. Finally, the outflow fluid mass  $\Delta m_j$  [M] and pressure head [L] were recorded for given interval of time  $\Delta t$  [T] once constant head was reached under saturated conditions. For each fluid, the volumetric flow rate  $Q_j$  [ $L T^{-3}$ ] was calculated as  $\Delta m_j / \rho_j \Delta t$  where  $\rho_j$  is the density of fluid [ $M L^{-3}$ ].

## Non-Newtonian Fluids

As xanthan gum is a highly efficient thickener for water-based solutions, a concentration of 0.1% by weight causes a significant increase in viscosity. Hence, xanthan gum solutions of 0.5 and 1  $g\ kg^{-1}$  ( $\pm 0.1\ g\ kg^{-1}$ ) concentrations were prepared by combining xanthan gum, deionized water, and sodium azide (0.1% by weight, to prevent biodegradation) in an electric kitchen blender, and blending until xanthan gum was fully dispersed. The mixture was then transferred to a sealed container and stirred with a laboratory electric stirrer for 48 h, before being centrifuged for 1 h at  $2000 \times g$  and vacuum filtered through a 2.5-mm, glass fiber filter. After filtration, the solution was stored in sealed container in the dark at  $5^\circ C$ . The final concentration was determined gravimetrically by evaporating an accurately weighed mass of the solution at  $105^\circ C$ . The power law viscosity model parameters for the 0.5 and 1  $g\ kg^{-1}$

xanthan gum concentrations were measured with a TA Instruments AR-G2 rotational rheometer with a cone-and-plate configuration. The samples were pre-sheared at  $1\ s^{-1}$  for 1 min, and then measurements were taken across a torque range of 0.05 to 500 N m at  $22^\circ C$ . The apparent viscosity and shear rate values output by the instrument were used to fit the power law model for each gum solution (Table 2). Note that both xanthan gum solutions had densities of  $1000\ g\ m^{-3}$ .

## Soil Columns

We conducted laboratory experiments using three different silica sands and three fluids (water and 0.5 and 1.0  $g\ kg^{-1}$  xanthan gum solutions). For the no. 12/20 and no. 20/30 silica sands, one, two, and three capillary tubes were used while only one capillary tube was used for no. 40/50 silica sand, making a total of seven different soil configurations. Therefore, in this investigation, a total of 21 experiments were conducted (i.e., seven soil–capillary tube

combinations  $\times$  three fluids). The experimental saturated flow results from water and each solution of xanthan gum were used as ANA-2 model inputs. For each soil–capillary tube combination, the pore structures of micropores and macropores (obtained from ANA-2 model using water and one non-Newtonian fluid at a time) were compared with results of pore size distributions from 2.5- to 3.5-cm soil sections using a Nikon XTH 225 ST high-resolution X-ray microcomputed tomography ( $\mu CT$ ) scanner. The  $\mu CT$  scanning was executed in the Shared Materials Instrumentation Facility (SMIF) at Duke University, with a resolution of between 11.9 to 18.9  $\mu m\ pixel^{-1}$ .

## Dual Pore Structure Calculations

Results from the  $\mu CT$  showed that the largest pores for the coarsest sand used (no. 12/20) were  $<0.20\ mm$ , with the other two sands (no. 20/30 and no. 40/50) having much smaller pores. Thus, the macropores were dominated by the size of the 0.75-mm capillary tubes used, and the micropores were estimated as the average contribution of the entire sand structure. The latter was estimated by discretizing the pore size distribution (assuming all pores are conducting vertically) of each sand into at least 100 pore-size

Table 2. Power law parameters of the two xanthum gum fluids.

| Concentration | $k$    | $\alpha$ |
|---------------|--------|----------|
| $g\ kg^{-1}$  | Pa s   |          |
| 0.5           | 1.2162 | 0.4269   |
| 1             | 1.8036 | 0.3638   |

groups per sand type, calculating the number of pores per group from the incremental change in pore volume, and computing the theoretical flow per group using the Hagen–Poiseuille equation to obtain the total theoretical flow,  $Q$  [ $L^3 T^{-1}$ ]. Thus, for each soil, the average corresponding pore radius  $R$  and number of pores  $X$  were estimated using the following system of equations:

$$\begin{cases} Q = \frac{X\pi\Delta P R^4}{8\mu L T} \\ \phi = \frac{X\pi R^2}{A_T} \end{cases} \quad [9]$$

Then we used the total theoretical flow to calculate an average micropore size given the total porosity of the sand as follows:

$$\begin{cases} R = \sqrt{\frac{8\mu L T Q}{\phi A_T \Delta P}} \\ X = \frac{\phi A_T}{\pi R^2} \end{cases} \quad [10]$$

The macropore (0.75 mm) and micropore radius (both referred to as experimental radii) were used to validate the ANA-2 macropore and micropore size estimates.

The weights or contributions to flow were also calculated from the experimental results of total saturated water flow ( $Q_1$ ) for each soil combination (sand plus  $M$  capillary tubes) by assuming that total flow ( $Q_1$ ) is equal to the sum of flow from the sand plus the capillary tubes, and realizing that the flow in the macropores (0.75 mm radius capillary tubes) can be calculated from the Hagen–Poiseuille equation. The resulting weights  $w_1$  and  $w_2$  (for micropores and macropores, respectively) add up to 1 and hereafter are referred to as experimental weights.

## Results and Discussion

Experimental flows for water ( $Q_1$ ) and xanthan gum fluid ( $Q_2$ ) were used to solve the different optimization problems under the three problem types. In Problem Type 1, the model was provided with the experimental radii of the two dominant porous structures (sand and capillary tubes) to solve for the corresponding

flow contribution weights of macropores ( $w_1$ ) and micropores ( $w_2$ ). In Problem Type 2, the model was provided with the experimental weights to solve for the corresponding radii of macropores ( $R_1$ ) and micropores ( $R_2$ ). In Problem Type 3, the corresponding radii and weights of the macropores and micropores were obtained without any additional inputs to the model. Results from the seven soil combinations under the three different problem types were used to evaluate the ANA-2 model ability to physically extract pore structural information that can be used in parameterizing dual-permeability models, using non-Newtonian fluids.

### Model Predictions under Problem Type 1

Table 3 summarizes the results of the simulations for all three sands and seven soil combinations (sand with one, two, or three capillary tubes) at different tortuosities under Problem Type 1. The weights (flow contributions) were obtained by the ANA-2 model given the experimental average pore radii representing the micropores (from scans) and the macropores (0.75 mm). Statistical differences between experimental and modeled weights were between 1 and 8% when each of the two pore structures contributed to at least 10% of the total flow. The model was not able to accurately capture the micropore contribution when macropores dominated the total flow (i.e., no. 20/30 sand with three capillary tubes and no. 40/50 sand with one capillary tube). In other words, when most of the flow passed through the macropore system, ANA-2 was not sensitive enough to catch the small fluxes in the matrix. However, the model correctly captured the macropore contributions of those two cases, with only 5 and 4% differences between modeled and experimentally calculated weights. The close correspondence between experimental and modeled macropore weights (1–8%) means that the model works well for the first problem type (when pore radii are known or assumed).

### Model Predictions under Problem Type 2

The ANA-2 model was next used to simulate the flow results under Problem Type 2 (Fig. 3). Here, experimental weights were provided and macropores were given a tortuosity of 1, while a wide range of hydraulic tortuosity models (Table 1) was tested

Table 3. Problem Type 1 summary.

| Type of sand | No. of macropores, $M$ | Tortuosity of sand<br>(between 1.2 and 3) | Weights by ANA-2 model |                    | Experimental weights |                    | Statistical difference† |                       |
|--------------|------------------------|---|------------------------|--------------------|----------------------|--------------------|-------------------------|-----------------------|
|              |                        |   | $w_{\text{micro}}$     | $w_{\text{macro}}$ | $w_{\text{micro}}$   | $w_{\text{macro}}$ | Diff <sub>micro</sub>   | Diff <sub>macro</sub> |
| %            |                        |   |                        |                    |                      |                    |                         |                       |
| No. 12/20    | 1                      | 1.224                                     | 64.4                   | 35.6               | 66.7                 | 33.3               | −0.034                  | 0.069                 |
|              | 2                      | 1.402                                     | 41.6                   | 58.4               | 43.0                 | 57.0               | −0.032                  | 0.024                 |
|              | 3                      | 1.807                                     | 22.3                   | 77.7               | 23.1                 | 76.9               | −0.034                  | 0.010                 |
| No. 20/30    | 1                      | 1.227                                     | 54.3                   | 45.7               | 50.1                 | 49.9               | 0.084                   | −0.084                |
|              | 2                      | 1.810                                     | 20.4                   | 79.6               | 19.3                 | 80.7               | 0.058                   | −0.014                |
|              | 3                      | 3.000                                     | 6.0                    | 94.0               | 1.2                  | 98.8               | 4.048                   | −0.049                |
| No. 40/50    | 1                      | 3.000                                     | 5.0                    | 95.0               | 1.5                  | 98.5               | 2.333                   | −0.036                |

† Statistical difference = (modeled − experimental)/experimental.

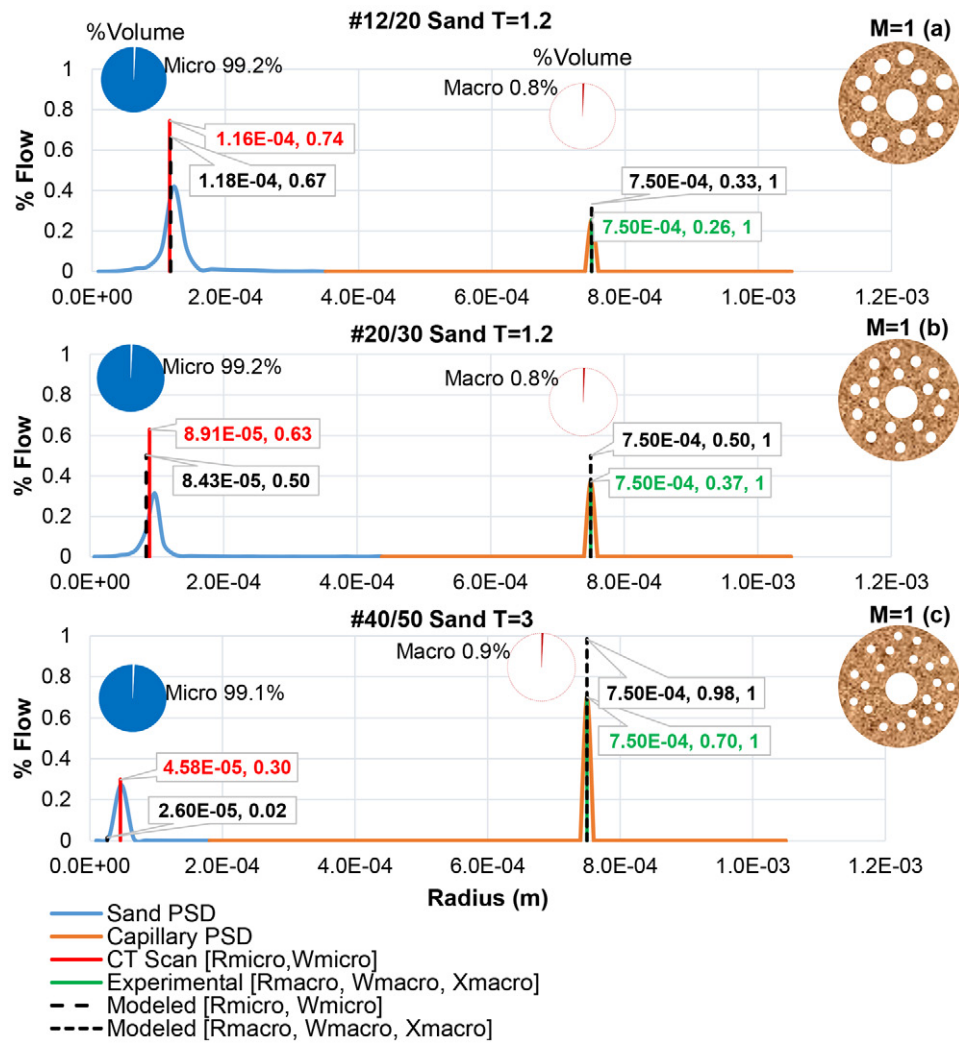


Fig. 3. Bimodal pore size distribution (PSD) in the dual-domain structure built with one capillary tube ( $M$ ) of 0.75-mm radius along with the (a) no. 12/20 silica sand of tortuosity  $T = 1.2$ , (b) no. 20/30 of  $T = 1.2$ , and (c) no. 40/50 of  $T = 3$ . Experimental results highlighted in red and green representing the porous structure in two points: the averaged micropore radius and corresponding weight ( $R_{\text{micro}}, w_{\text{micro}}$ ) using a computed tomography (CT) scan, and the actual macropore radius and its corresponding weight and number ( $R_{\text{macro}}, w_{\text{macro}}, X_{\text{macro}}$ ), respectively. Similarly, the two simulated radii predicted by the ANA model are highlighted in black with the predefined set of weights estimated experimentally using the Hagen–Poiseuille equation.

for the micropores with tortuosity values ranging from 1.2 to 3. To highlight the contribution to flow, Fig. 3 plots the percentage flow vs. pore size in an attempt to show the large contribution to flow from macropores (33–98% of total flow) despite the fact that they all contributed <1% of total pore space in the three cases. Furthermore, the porosity and volumetric contribution of micropores and macropores are highlighted on each graph by two circles showing the corresponding percentage volume of the micropores and macropores to emphasize the micro and macro contribution to the total porosity.

Comparisons between modeled and experimental radii reveal the model's ability to estimate the effective pore sizes of the dual structure. The model accurately estimated the 0.75-mm radius of the capillary tube for the three dual soil configurations. Moreover, the model correctly captured the actual micropore radius of the no. 12/20 and no. 20/30 sand, with only 1 and 5% differences between modeled and experimental sizes, respectively.

However, the model was not able to capture the micropore size when macropores dominated the total flow (>90% in the case no. 40/50 sand), leading to underestimations in the micropore size estimate.

As the number of capillary tubes increased from only one tube to two or three tubes, the model's ability to provide an accurate estimate of the macropores radii size was reduced. This is demonstrated in Fig. 4, which shows model estimates for the no. 12/20 and no. 20/30 silica soils with two and three capillary tubes. The no. 40/50 sand experiment with two and three capillary tubes was disregarded, since macropores dominated flow with 98% contribution to flow with only one 0.75-mm tube. In all cases, the model assumed that the macropore domain was composed of a single pore, thus not identifying experiments where the soil had two or three capillary tubes. In those instances, the model estimated a larger pore size to match the assigned weights needed for the macropore contribution to flow (hydrologically

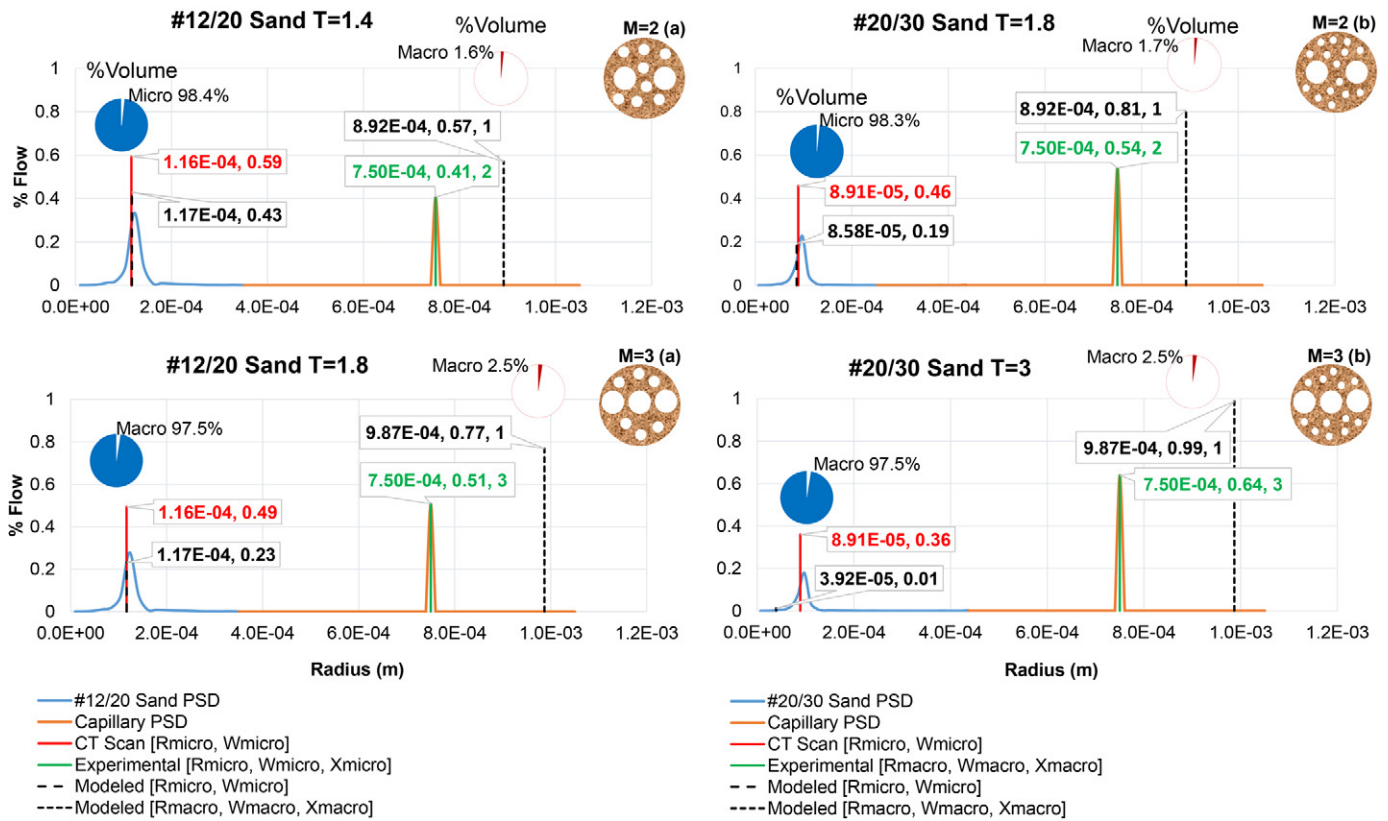


Fig. 4. Bimodal pore size distribution (PSD) in the dual-domain structure built with two and three capillary tubes ( $M$ ) of 0.75-mm radius with (a) no. 2/20 and (b) no. 20/30 silica sand of tortuosity  $T$ . Experimental results highlighted in red and green representing the porous structure in two points: the averaged micropore radius and corresponding weight ( $R_{\text{micro}}, w_{\text{micro}}$ ) using a computed tomography (CT) scan, and the actual macropore radius and its corresponding weight and number ( $R_{\text{macro}}, w_{\text{macro}}, X_{\text{macro}}$ ), respectively. Similarly, the two simulated radii predicted by the ANA model are highlighted in black with the predefined set of weights estimated experimentally using the Hagen–Poiseuille equation.

relatively equivalent to the two or three 0.75-mm tubes). Still, the model is simulating a similar hydraulic behavior as the real soil, with the similar relative contributions of the micropore and macropore domains to total flow, at slightly smaller percentage volume or porosity for macropores (Table 4). This result highlights an area of potential improvement on the model that will require more knowledge (or assumptions) on the pore structure and its tortuosity and connectivity.

### Model Predictions under Problem Type 3

Although Problem Types 1 and 2 generate unique solutions, there is no unique solution under Problem Type 3, which solves two equations with four unknowns (radii  $R_{\text{micro}}$  and  $R_{\text{macro}}$  and their corresponding weights  $w_{\text{micro}}$  and  $w_{\text{macro}}$ ) that vary simultaneously. Therefore, we investigated the stability of the obtained solutions to check whether they remain within acceptable margins from the experimental results for a wide range of starting points

Table 4. Problem Type 2 summary.

| Macropore parameter†                     | $M = 1\ddagger$       |                       | $M = 2$               |                       | $M = 3$               |                       |
|--|-----------------------|-----------------------|-----------------------|-----------------------|-----------------------|-----------------------|
|  | Experiment            | ANA model             | Experiment            | ANA model             | Experiment            | ANA model             |
| $R_{\text{macro}}$ (m)                   | $7.50 \times 10^{-4}$ | $7.50 \times 10^{-4}$ | $7.50 \times 10^{-4}$ | $8.92 \times 10^{-4}$ | $7.50 \times 10^{-4}$ | $9.87 \times 10^{-4}$ |
| $X_{\text{macro}}$                       | 1                     | 1                     | 2                     | 1                     | 3                     | 1                     |
| $K_{\text{macro}}$ ( $\text{m s}^{-1}$ ) | $2.20 \times 10^{-3}$ | $2.20 \times 10^{-3}$ | $4.40 \times 10^{-3}$ | $4.40 \times 10^{-3}$ | $6.60 \times 10^{-3}$ | $6.60 \times 10^{-3}$ |
| Volume (%)                               |                       |                       |                       |                       |                       |                       |
| No. 12/20 sand                           | 0.82                  | 0.82                  | 1.65                  | 1.16                  | 2.47                  | 1.43                  |
| No. 20/30 sand                           | 0.84                  | 0.84                  | 1.65                  | 1.16                  | 2.51                  | 1.43                  |
| No. 40/50 sand                           | 0.87                  | 0.87                  |                       |                       |                       |                       |

†  $R_{\text{macro}}$  is the radius,  $X_{\text{macro}}$  is the number, and  $K_{\text{macro}}$  is the hydraulic conductivity of macropores.  $K_{\text{macro}} = (\pi \rho g X R^4) / (8 \mu A_T)$ . Volume (%) =  $(\pi X R^2) / (\phi A_T)$ , where  $\phi$  is the porosity of the porous media [ $\text{m}^3 \text{m}^{-3}$ ].

‡  $M$  is number of capillary tubes.



and runs. The starting points are the initial unknown values, generated randomly and provided to the optimizer for the following evaluation. We performed 25 runs on each scenario from different and randomly selected starting points. The results of flow and pore structure predicted under Problem Type 3 were clustered around the experimental flow contributions and radii of macro- and micropores for the three dual structures soil combinations. (Fig. 5; Table 5).

As the number of capillary tubes increased from one tube to two or three tubes, the ANA-2 model was constantly capable of solving Problem Type 3 with representative radii of micropores clustered around the average radii of the actual pores (Fig. 6). However, the model continued to predict the presence of a single macropore (instead of two or three macropores), which resulted in calculating a larger macropore radius to accommodate the flow of the other macropores (note that the relationship is not linear, since flow is proportional to the fourth power of the pore

size, whereas porosity is proportional to the second power of pore size). Both structures (the one obtained by the ANA-2 model and that obtained by scanning) were hydraulically equivalent for all the soils tested. This behavior was previously encountered in the Problem Type 2 analysis, which emphasizes the consistency in results of the ANA-2 model between the different optimization problems.

As a final assessment of the stability of results obtained for Problem Type 3 given the infinite theoretical number of solutions, additional random runs were conducted on no. 12/20 soil assembled with one capillary tube (for the case of  $M = 1$ ) from different starting points ( $n$ ). Modeled hydraulic parameters (i.e., radii and weight/flow contributions) of the macro- and micropores were summarized as a probability density functions for  $n = 30, 60, 90, 120, 240$ , and 500 random runs. Figure 7 shows, for  $n = 30, 60, 90, 120, 240$ , and 500 random runs, the actual micro (left) and macro (right) radius in red, and the mean of modeled

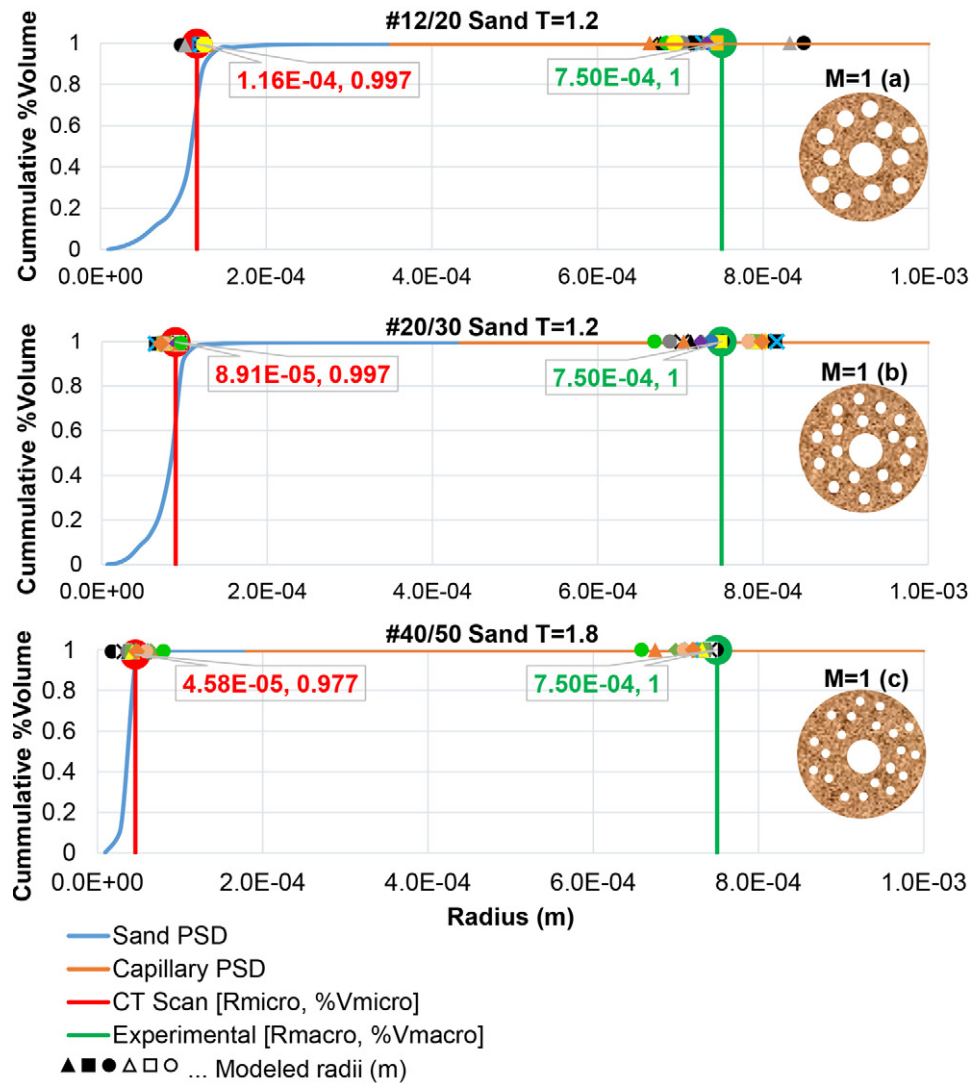


Fig. 5. Cumulative pore size distribution (PSD) of the dual-domain structure built with one capillary tube ( $M$ ) of 0.75-mm radius with (a) no. 12/20, (b) no. 20/30, and (c) no. 40/50 silica sand of tortuosity  $T$ . Red and green circles signifying the experimental averaged micropore radius and corresponding volume ( $R_{\text{micro}}$ ,  $\%V_{\text{micro}}$ ) using a computed tomography (CT) scan, and the experimental (actual) macropore radius and its corresponding volume ( $R_{\text{macro}}$ ,  $\%V_{\text{macro}}$ ), respectively. Results of the 25 ANA-2 model runs plotted through a wide array of symbols.

Table 5. Problem Type 3 summary.

| Sand           | Parameter†                        | $M = 1\ddagger$       |                       | $M = 2$               |                       | $M = 3$               |                       |
|----------------|-----------------------------------|-----------------------|-----------------------|-----------------------|-----------------------|-----------------------|-----------------------|
|                |                                   | Experiment            | ANA model             | Experiment            | ANA model             | Experiment            | ANA model             |
| No. 12/20 sand | $R_{\text{micro}}$ (m)            | $1.16 \times 10^{-4}$ | $1.19 \times 10^{-4}$ | $1.16 \times 10^{-4}$ | $1.19 \times 10^{-4}$ | $1.16 \times 10^{-4}$ | $1.20 \times 10^{-4}$ |
|                | $R_{\text{macro}}$ (m)            | $7.50 \times 10^{-4}$ | $7.25 \times 10^{-4}$ | $7.50 \times 10^{-4}$ | $8.83 \times 10^{-4}$ | $7.50 \times 10^{-4}$ | $9.43 \times 10^{-4}$ |
|                | $X_{\text{macro}}$                | 1                     | 1                     | 2                     | 1                     | 3                     | 1                     |
|                | Equivalent $R_{\text{macro}}$ (m) | $7.50 \times 10^{-4}$ | $7.25 \times 10^{-4}$ | $7.50 \times 10^{-4}$ | $7.43 \times 10^{-4}$ | $7.50 \times 10^{-4}$ | $7.17 \times 10^{-4}$ |
|                | $w_{\text{micro}}$ (%)            | 66.67                 | 70.61                 | 42.99                 | 44.65                 | 23.13                 | 35.03                 |
|                | $w_{\text{macro}}$ (%)            | 33.33                 | 29.39                 | 57.01                 | 55.35                 | 76.87                 | 64.97                 |
| No. 20/30 sand | $R_{\text{micro}}$ (m)            | $8.91 \times 10^{-5}$ | $8.38 \times 10^{-5}$ | $8.91 \times 10^{-5}$ | $8.44 \times 10^{-5}$ | $8.91 \times 10^{-5}$ | $6.05 \times 10^{-5}$ |
|                | $R_{\text{macro}}$ (m)            | $7.50 \times 10^{-4}$ | $7.38 \times 10^{-4}$ | $7.50 \times 10^{-4}$ | $8.59 \times 10^{-4}$ | $7.50 \times 10^{-4}$ | $9.66 \times 10^{-4}$ |
|                | $X_{\text{macro}}$                | 1                     | 1                     | 2                     | 1                     | 3                     | 1                     |
|                | Equivalent $R_{\text{macro}}$ (m) | $7.50 \times 10^{-4}$ | $7.38 \times 10^{-4}$ | $7.50 \times 10^{-4}$ | $7.22 \times 10^{-4}$ | $7.50 \times 10^{-4}$ | $7.34 \times 10^{-4}$ |
|                | $w_{\text{micro}}$ (%)            | 50.13                 | 55.46                 | 19.27                 | 34.62                 | 1.19                  | 10.00                 |
|                | $w_{\text{macro}}$ (%)            | 49.87                 | 44.54                 | 80.73                 | 65.38                 | 98.81                 | 90.00                 |
| No. 40/50 sand | $R_{\text{micro}}$ (m)            | $4.58 \times 10^{-5}$ | $4.85 \times 10^{-5}$ |                       |                       |                       |                       |
|                | $R_{\text{macro}}$ (m)            | $7.50 \times 10^{-4}$ | $7.20 \times 10^{-4}$ |                       |                       |                       |                       |
|                | $X_{\text{macro}}$                | 1                     | 1                     |                       |                       |                       |                       |
|                | Equivalent $R_{\text{macro}}$ (m) | $7.50 \times 10^{-4}$ | $7.20 \times 10^{-4}$ |                       |                       |                       |                       |
|                | $w_{\text{micro}}$ (%)            | 1.50                  | 19.12                 |                       |                       |                       |                       |
|                | $w_{\text{macro}}$ (%)            | 98.50                 | 80.88                 |                       |                       |                       |                       |

†  $R_{\text{micro}}$  is the micropore radius,  $R_{\text{macro}}$  is the macropore radius,  $X_{\text{macro}}$  is the number of macropores, and  $w_{\text{micro}}$  and  $w_{\text{macro}}$  are the weights of micro- and macropores, respectively.

‡  $M$  is number of capillary tubes.

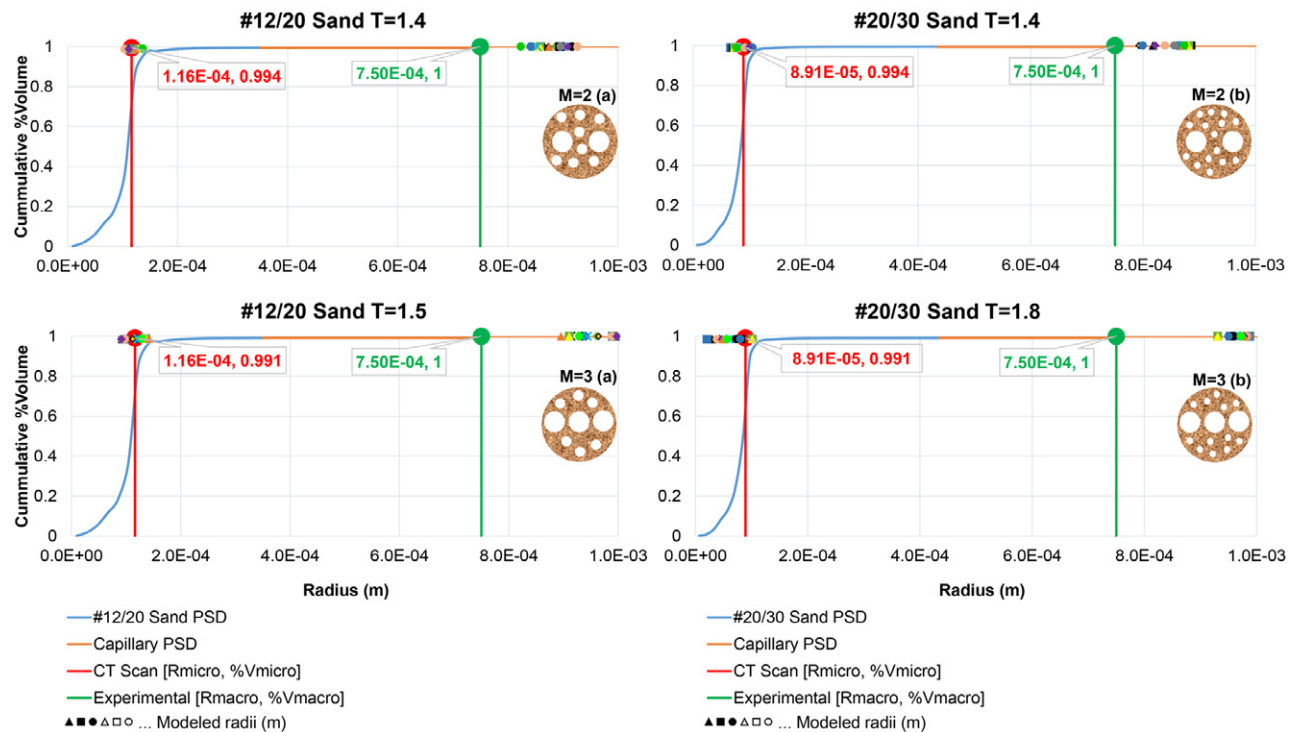


Fig. 6. Cumulative pore size distribution (PSD) of the dual-domain structure built with two and three capillary tubes ( $M$ ) of 0.75-mm radius with (a) no. 12/20 and (b) no. 20/30 silica sand of tortuosity  $T$ . Red and green circles signifying the experimental averaged micropore radius and corresponding volume ( $R_{\text{micro}}$ ,  $\%V_{\text{micro}}$ ) using a computed tomography (CT) scan, and the experimental (actual) macropore radius and its corresponding volume ( $R_{\text{macro}}$ ,  $\%V_{\text{macro}}$ ), respectively. Results of the 25 ANA-2 model runs plotted through a wide array of symbols.

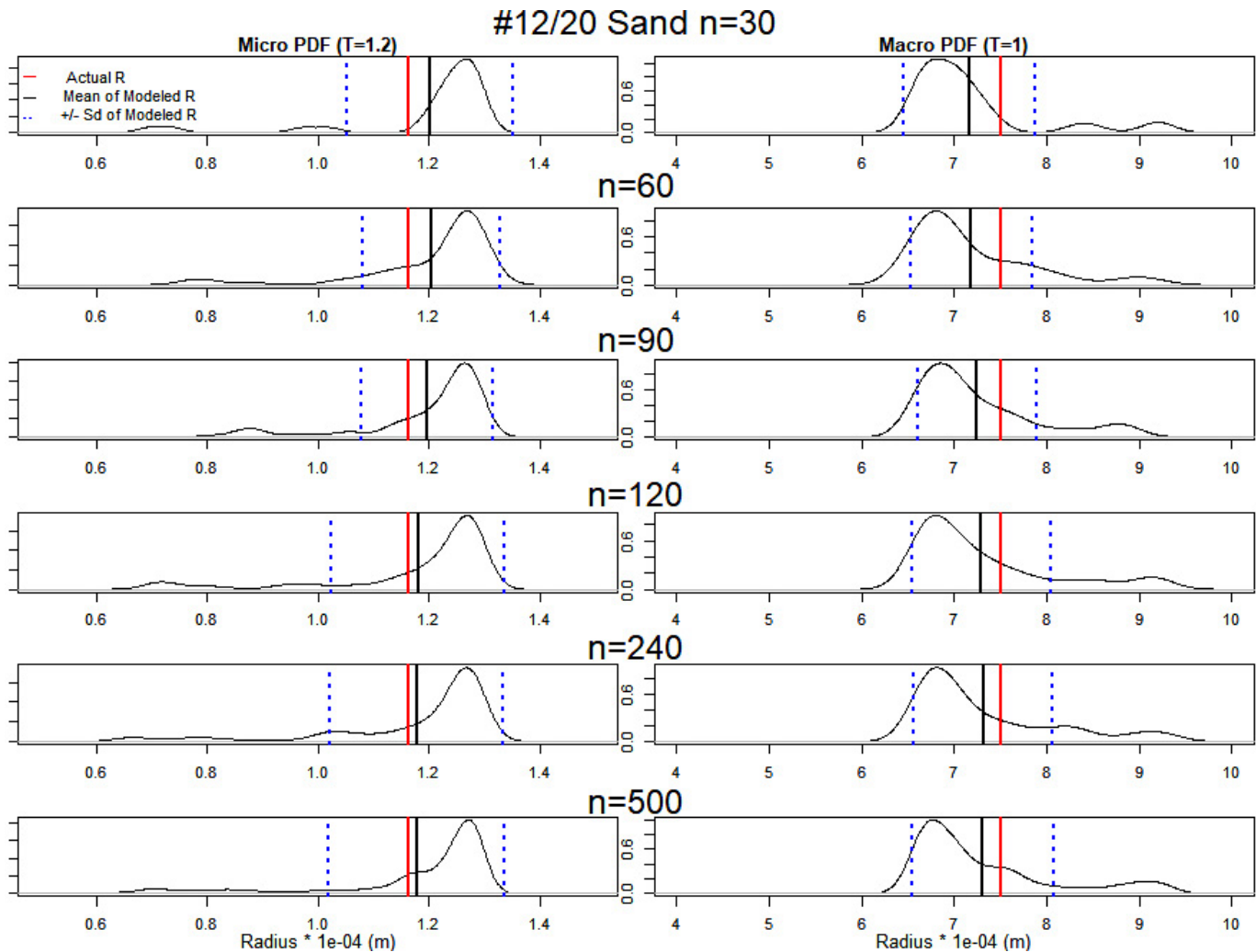


Fig. 7. Probability density function (PDF) for the micro and macro modeled radii  $R$  of the dual-domain structure built with one capillary tube of 0.75-mm radius of tortuosity of  $T = 1$  and no. 12/20 silica sand of tortuosity  $T = 1.2$ .

radii as well as the range of 1 SD. The results seem encouraging and stable. For example, out of 500 random runs, the actual micropore radius ( $1.16 \times 10^{-4}$  m) was estimated with a mean of  $\sim 1.19 \times 10^{-4}$  m with a range of around  $1.07$  to  $1.33 \times 10^{-4}$  m for  $\pm 1$  SD. Furthermore, Fig. 7 shows that obtaining a close estimate of the mean did not require a large number of runs and is consistently close to the actual mean in both macro- and micropores.

Similarly, Fig. 8 shows, for  $n = 30, 60, 90, 120, 240$ , and 500 random runs, the actual contributions to flow for the micro- (left) and macropores (right) in red, and the mean of modeled weights as well as the range of 1 SD. Results were encouraging, since the model showed relatively close estimates to the experimental weight values with the means of experimental and modeled weights within  $\sim 5\%$ .

## Summary and Conclusions

This study developed a new physically based model to extract dual-permeability parameters from dual-permeability soils using two solutions, including water and one non-Newtonian fluid. The

method is relatively cheap and simple, requiring limited inputs and simple experimental procedures. The corresponding model then characterizes two effective pore sizes, one for the macropores of higher permeability, and one for the micropores of lower permeability. The efficiency of the proposed method was validated through a sequence of infiltration experiments with porous dual-domain samples made out of silica sand (as the micropore domain) and different numbers of capillary tubes (as the macropore domain). Results illustrated the ability of the model to characterize and quantify the representative macro- and micropores using only flows generated from two saturated infiltration experiments.

Overall, the ANA-2 model was capable of predicting the micropore and macropore flow characteristics of dual structured soils given only the total flows from water and one non-Newtonian fluid. This effectiveness was demonstrated by the results under Problem Type 1 (Table 3), where the ANA-2 model was capable of predicting the flow contributions (weights of macro- and microstructures) compared with the weights estimated using the Hagen–Poiseuille equation. A similar conclusion can be inferred

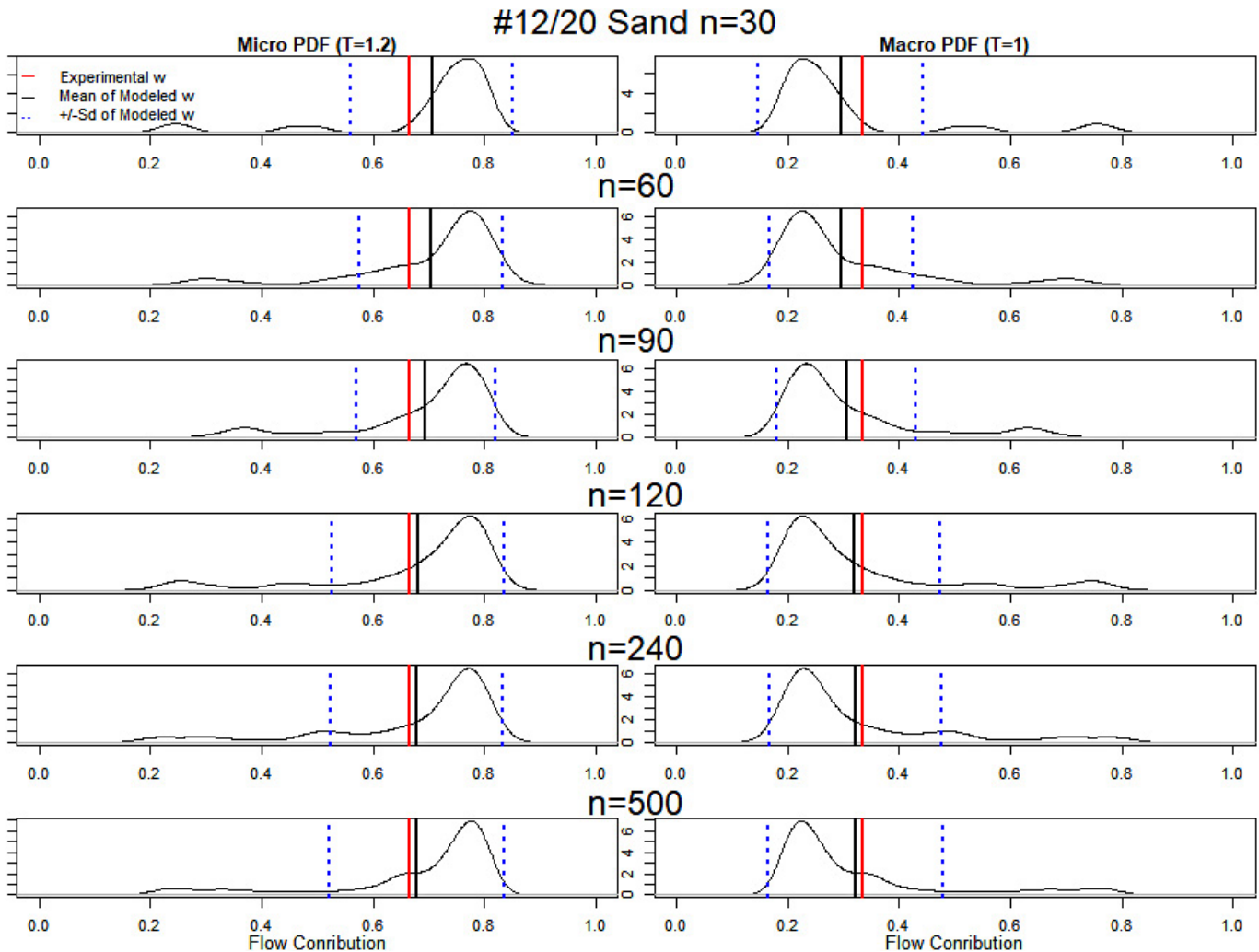


Fig. 8. Probability density function (PDF) for the micro and macro modeled weights  $w$  of the dual-domain structure built with one capillary tube of 0.75-mm radius of  $T = 1$  and no. 12/20 silica sand of tortuosity  $T = 1.2$ .

from the model's estimation of the pore structure of the dual-permeability soils under Problem Type 2, particularly when one capillary tube was used (Fig. 3). In addition, the ANA-2 model provides an effective characterization of the same dual soil configuration (i.e.,  $M = 1$ ) under Problem Type 3 analysis, despite the infinite theoretical number of solutions (Fig. 5). However, the model was less successful in predicting the macropore structure when more than one capillary tube was used (Fig. 4). The model performed better when the soil behaved like a dual-permeability soil and was not able to accurately capture micropore characteristics when the flow was dominated by macropores (>95% of flow). These results revealed that the model was biased more to flow than to porosity and structure, as it successfully characterized pore hydraulics even when failing to correctly estimate macropore numbers and sizes. Thus, although the model provides an important step forward in flow modeling, further refinements are required for the model to better predict the pore structure.

The model was only validated here for circular macropore geometries. However, the model equations were also derived for

the planar macropore geometry (Supplemental Material), and the solver (can be obtained from the corresponding author) is equipped to solve both geometries. As those tools are now available, we hope that this will be the topic of future research. Another area of additional research should target the sensitivity of the model to the tortuosity model choice and perhaps add or improve the model formulation to predict a reasonable range of tortuosity. Finally, even though X-ray microcomputed tomography ( $\mu$ CT) scanning can provide high-resolution imaging of pore sizes and connectivity, our proposed method provides a major advantage in its ability to assess soils at multiple scales and be conducted in the field. We expect that future applications of this method will provide new insight into the scale dependence of macropore effects on hydraulic conductivity.

### Supplemental Material

The supplemental material includes detailed derivations of: (i) the velocity and flow equations between parallel fixed plates for the power law viscosity model, and (ii) the  $2 \times 2$  matrix for the two



configurations: micropores represented by cylindrical pore geometries with macropores either in cylindrical or planar pore geometries.

## Acknowledgments

This study was supported by the University Research Board of the American University of Beirut.

## References

- Abou Najm, M.R., and N.M. Atallah. 2016. Non-Newtonian fluids in action: Revisiting hydraulic conductivity and pore size distribution of porous media. *Vadose Zone J.* 15(9). doi:10.2136/vzj2015.06.0092
- Abou Najm, M.R., J.D. Jabro, W.M. Iversen, R.H. Mohtar, and R.G. Evans. 2010. New method for the characterization of three-dimensional preferential flow paths in the field. *Water Resour. Res.* 46:W02503. doi:10.1029/2009WR008594
- Ahmadi, M.M., S. Mohammadi, and A.N. Hayati. 2011. Analytical derivation of tortuosity and permeability of monosized spheres: A volume averaging approach. *Phys. Rev. E* 83:026312. doi:10.1103/PhysRevE.83.026312
- Atallah, N.M., and M.R. Abou Najm. 2019. Characterization of synthetic porous media using non-Newtonian fluids: Experimental evidence. *Eur. J. Soil Sci.* 70:257–267. doi:10.1111/ejss.12746
- Berryman, J.G. 1981. Elastic wave propagation in fluid-saturated porous media. *J. Acoust. Soc. Am.* 69:416–424. doi:10.1121/1.385457
- Beven, K.J. 1991. Modeling preferential flow: An uncertain future? In: T.J. Gish and A. Shirmohannadi, editors, *Preferential flow*. Am. Soc. Agric. Eng., St. Joseph, MI. p. 1–11.
- Beven, K., and P. Germann. 1982. Macropores and water flow in soils. *Water Resour. Res.* 18:1311–1325. doi:10.1029/WR018i005p01311
- Busch, J., T. Meißner, A. Potthoff, and S.E. Oswald. 2014. Transport of carbon colloid supported nanoscale zero-valent iron in saturated porous media. *J. Contam. Hydrol.* 164:25–34. doi:10.1016/j.jconhyd.2014.05.006
- Carey, G.R., E.A. McBean, and S. Feenstra. 2016. Estimating tortuosity coefficients based on hydraulic conductivity. *Groundwater* 54:476–487. doi:10.1111/gwat.12406
- Carman, P.C. 1937. Fluid through granular beds. *Trans. Inst. Chem. Eng.* 15:155–166.
- Comba, S., D. Dalmazzo, E. Santagata, and R. Sethi. 2011. Rheological characterization of xanthan suspensions of nanoscale iron injection in porous media. *J. Hazard. Mater.* 185:598–605. doi:10.1016/j.jhazmat.2010.09.060
- Di Federico, V., M. Pinelli, and R. Ugarelli. 2010. Estimates of effective permeability for non-Newtonian fluid flow in randomly heterogeneous porous media. *Stochastic Environ. Res. Risk Assess.* 24:1067–1076. doi:10.1007/s00477-010-0397-9
- Du Plessis, J.P., and J.H. Masliyah. 1991. Flow through isotropic granular porous media. *Transp. Porous Media* 6:207–221. doi:10.1007/BF00208950
- Duda, A., Z. Koza, and M. Matyka. 2011. Hydraulic tortuosity in arbitrary porous media flow. *Phys. Rev. E* 84:036319. doi:10.1103/PhysRevE.84.036319
- Dullien, F.L. 1975. Single phase flow through porous media and pore structure. *Chem. Eng. J.* 10:1–34. doi:10.1016/0300-9467(75)88013-0
- Gastone, F., T. Tosco, and R. Sethi. 2014. Guar gum solutions for improved delivery of iron particles in porous media (Part 1): Porous medium rheology and guar gum-induced clogging. *J. Contam. Hydrol.* 166:23–33. doi:10.1016/j.jconhyd.2014.06.013
- Gerke, H.H., and M.Th. van Genuchten. 1993. A dual-porosity model for simulating the preferential movement of water and solutes in structured porous media. *Water Resour. Res.* 29:305–319. doi:10.1029/92WR02339
- Jarvis, N.J. 1994. The MACRO model ver. 3.1: Technical description and sample simulations. Reports and dissertations. Vol. 19. Swedish Univ. Agric. Sci., Uppsala, Sweden.
- Jarvis, N.J. 2007. A review of non-equilibrium water flow and solute transport in soil macropores: Principles, controlling factors and consequences for water quality. *Eur. J. Soil Sci.* 58:523–546. doi:10.1111/j.1365-2389.2007.00915.x
- Köhne, J.M., S. Köhne, and H. Gerke. 2002. Estimating the hydraulic functions of dual-permeability models from bulk soil data. *Water Resour. Res.* 38(7). doi:10.1029/2001WR000492
- Larsson, M.H., and N.J. Jarvis. 1999. Evaluation of a dual-porosity model to predict field-scale solute transport in a macroporous soil. *J. Hydrol.* 215:153–171. doi:10.1016/S0022-1694(98)00267-4
- Lewandowska, J., A. Szymkiewicz, K. Burzyński, and M. Vauclin. 2004. Modeling of unsaturated water flow in double porosity soils by the homogenization approach. *Adv. Water Resour.* 27:283–296. doi:10.1016/j.advwatres.2003.12.004
- Matyka, M., A. Khalili, and Z. Koza. 2008. Tortuosity-porosity relation in porous media flow. *Phys. Rev. E* 78:026306. doi:10.1103/PhysRevE.78.026306
- Mauret, E., and M. Renaud. 1997. Transport phenomena in multi-particle systems: I. Limits of applicability of capillary model in high voidage beds-application to fixed beds of fibers and fluidized beds of spheres. *Chem. Eng. Sci.* 52:1807–1817. doi:10.1016/S0009-2509(96)00499-X
- Moldrup, P., T. Olesen, T. Komatsu, P. Schjonning, and D.E. Rolston. 2001. Tortuosity, diffusivity and permeability in the soil liquid and gaseous phases. *Soil Sci. Soc. Am. J.* 65:613–623. doi:10.2136/sssaj2001.653613x
- Mota, M., J.A. Teixeira, W.R. Bowen, and A. Yelshin. 2001. Binary spherical particle mixed bed: Porosity and permeability relationship measurement. *Trans. Filtr. Soc.* 1:101–106.
- Šimůnek, J., N.J. Jarvis, M.Th. van Genuchten, and A. Gardenas. 2003. Review and comparison of models for describing non-equilibrium and preferential flow and transport in the vadose zone. *J. Hydrol.* 272:14–35. doi:10.1016/S0022-1694(02)00252-4
- Stewart, R.D., M.R. Abou Najm, D.E. Rupp, and J.S. Selker. 2014. Nondestructive quantification of macropore volume using shear-thinning fluid. *Soil Sci. Soc. Am. J.* 78:445–453. doi:10.2136/sssaj2013.08.0346
- Tosco, T., F. Gastone, and R. Sethi. 2014. Guar gum solutions for improved delivery of iron particles in porous media (Part 2): Iron transport tests and modeling in radial geometry. *J. Contam. Hydrol.* 166:34–51. doi:10.1016/j.jconhyd.2014.06.014
- van Genuchten, M.Th., D.E. Rolston, and P.F. Germann, editors. 1990. *Transport of water and solutes in macropores*. Geoderma 46:1–297.